2-D Wide-Angle Multi-Beam Flat GRIN Lens with A High Aperture Efficiency

Li-Zhao Song, Maral Ansari, Pei-Yuan Qin, *Senior Member, IEEE,* Stefano Maci, *Fellow, IEEE,* Jia Du, and Y. Jay Guo, *Fellow, IEEE*

***Abstract*—High-aperture-efficiency 2-dimensional (2-D) multi-beam flat gradient-index (GRIN) lenses are developed in this work. New methods based on bifocal analysis are found to determine the refractive-index profile of the lens as well as feed positions along a circular feed locus to enable independent wide-angle multi-beam radiations. Distinct formulas for the GRIN profile are provided for two different purposes: i) multi-beam with good average performance in all azimuthal planes or ii) radiation performance optimized in a specific azimuthal plane. The latter solution requires a GRIN variation in both azimuthal and radial variables. Subwavelength triple-metal-layer unit cells are designed to emulate the local refractive indices. A 2-D multi-beam GRIN lens, fed by 13-modules of 2x2 patch arrays displaced along *xoz* and *yoz* focus loci, has been successfully simulated, fabricated, and measured. Wide-angle multi-beam radiations have been obtained with a beam coverage of around ±45° in both *xoz* and *yoz* planes. The multi-beam radiation patterns are stable in a 22.2% bandwidth from 12 GHz to 15 GHz. The beam-scanning losses in this operating band are 1-2.6 dB and 2.1-3.9 dB in *xoz* and *yoz* planes, respectively. The measured peak realized gain is 22.3 dBi at 13.4 GHz, corresponding to an aperture efficiency of 66.4%.**

***Index Terms*— 2-D multi-beam, GRIN lens, high-efficiency, wide-angle beam scanning.**

I. Introduction

HIGH-GAIN multi-beam antennas are very promising candidates for long-distance communications for the current fifth generation (5G) and beyond wireless systems [1], as they can compensate for high path losses while facilitating multiple connections to distributed nodes located in a wide spatial range [2]-[4]. In this context, multi-beam antennas have been widely investigated, including lens antennas [5]-[6], transmitarray/reflectarray antennas [7]-[9], and microstrip arrays fed by beamforming networks [10]-[11], etc. Among them, lens antennas have attracted substantial interests due to their merits of wide band, high gain and high aperture efficiency.

There are two fundamental categories of lenses, namely homogeneous and inhomogeneous lenses [12]. The traditional homogeneous lens is constituted by a single pure dielectric material designed with a specific shape based on geometrical optics, e.g., convex and concave lenses. Despite its advantages of very large bandwidth and high efficiency, the homogeneous lenses exhibit a bulky and typically heavy configuration, especially at low frequencies. On the other hand, the inhomogeneous lens engineered with a gradient refractive-index profile can be developed using advanced 3-D printing and PCB manufacturing technologies, leading to a lighter and lower-profile structure at a reduced fabrication cost. Furthermore, inhomogeneous lenses provide the possibility of flat interface and more degrees of freedom to design the aperture efficiency. Some typical inhomogeneous lenses include Fresnel lenses [13]-[14], half Maxwell fish-eye lenses [15] and Luneburg lenses [16]-[18]. However, most of them have inherently 3-D configurations (e.g., sphere), thereby posing great challenges for them to be mounted onto the communications platforms. On the other hand, the flat version of them cannot be directly used as aperture antennas. To address this challenge, substantial efforts have been devoted to develop flat gradient-index (GRIN) lenses based on transformation optics [19]-[20], ray optics [21]-[25] and field transformations [26]. Many methods are developed to enhance its operating bandwidth and aperture efficiency with small refractive-index errors across the lens aperture.

To date, there have been a few reported multi-beam/beam-scanning flat GRIN lenses in open literature [27]-[33]. In [28], a dual-polarized flat Luneburg lens is reported at 10 GHz. By placing feed patch antennas along a straight trajectory, multiple beams can be achieved in an angular range of ±54° with scanning losses of 0.7 dB and 2.2 dB for two polarizations, respectively. The reported aperture efficiency is 21.2%. In [29], an all-dielectric flat Luneburg lens is developed at 10 GHz. A horn antenna can be moved along a straight trajectory to feed the lens, showing a beam-scanning range of ±34° and a scanning loss of 2 dB. The peak aperture efficiency is 67%. In [30], miniaturized frequency selective surfaces (FSS) elements are employed to constitute a flat GRIN lens fed by patch antennas at 9 GHz. The patch antenna can be moved along a straight trajectory for radiating multiple beams in an angular range of ±45° with a scanning loss of about 3 dB. The peak aperture efficiency is around 38%. In [31], a millimeter-wave flat GRIN lens is designed and fed by an open waveguide. By moving the feed along a straight trajectory, the radiating beam can be scanned to ±48° with a scanning loss of 4.6 dB at 60 GHz. The measured aperture efficiency is indirectly calculated as 27.4%. Moreover, a double-layer planar metasurface lens is proposed in [32] at 28 GHz. Seven SIW-fed stacked patch antennas are placed along a straight trajectory to excite multiple beams. A beam coverage of ±27° with a scanning loss of 3.7

This work was supported by the Australian Research Council Discovery Program under Grant DP 220101158 and DP230101955. This work was also supported by Italian Ministry of research (Project of Research of National Interest on “Metasurface Antennas, Prot. 2017S29ZLA).

dB is realized. The aperture efficiency is 24.5%. In [33], feed corrective lenslets are investigated to squint the radiation beam of feed horn towards lens center to reduce spillover losses. Besides, they can translate the feed phase center from a flat surface to Petzval surface. This way, a wide beam range of ±53° is realized with a beam scanning loss of around 5.5 dB. The peak aperture efficiency is 74% at 18 GHz. It should be noted that all the reported flat GRIN lenses scan their beams in one-dimensional (1-D) plane, although some of them have potentials to support two-dimensional (2-D) beam scanning, owing to their rotationally symmetrical lens profiles.

Based on the above literature review, for most designs with larger than ±45° beam coverages within a 3-dB gain drop, the peak aperture efficiencies are lower than 40%. However, for the designs with greater than 60% aperture efficiencies, they have either a small beam coverage or a high scanning loss. Therefore, there is a technology gap to achieve flat GRIN lenses with both high aperture efficiencies and good 2-D multi-beam/ beam-scanning capabilities.

In this work, we use the bifocal analysis method to design a flat GRIN lens that can scan over a large aperture or generate multiple beams with a high efficiency and a low scanning loss. It should be noted that there have been some other reported multi-beam dielectric lenses based on bifocal analysis [34]-[36]. However, the shapes of inner and outer lens surfaces of these designs were utilized as design freedoms, leading to curved lens contours. Different from the conventional flat GRIN lens design methods, our design processes are described next:

i) The GRIN profile for a flat lens configuration is found analytically by using a congruence of optical ray-paths for an approximately linear phase on the aperture; this phase can generate oblique beams at the extreme of the scanning angle range.
ii) The corresponding feed locus is theoretically determined as an arc. The combination of the refractive-index profile and the circular feed locus enables significant improvement in the 2-D beam-scanning performance.
iii) The method described in ii) is successively adapted to realize enhanced beam-scanning performance along one specific principal plane with the use of a refractive-index profile along both radial and azimuthal coordinates.

Finally, a 2-D multi-beam GRIN lens prototype, with totally 13 feed patch arrays arranged in two orthogonal planes, is fabricated and measured. To the authors' best knowledge, this is the first time that a 2-D multi-beam flat GRIN lens is implemented by multilayer metasurfaces and validated experimentally. Besides, good radiation performance in terms of the scanning capability and the aperture efficiency have been achieved. Compared to the conventional 3-D spherical Luneburg lenses, the proposed design may have a similar overall minimal enveloping spherical surface. However, the weight of the present solution is significantly lower. It can be easily mounted on and aligned to planar platforms without protruding from the surface. Besides, its lens aperture can be easily implemented by low-cost Print Circuit Board (PCB) technology. It should be noted that some very early research findings of multi-beam GRIN lens with limited preliminary simulation results were reported in authors' recent conference paper [37]. However, the current work presents comprehensive design solutions and validations with both simulation and measurement results.

The presentation of the paper is organized as follows. Section II presents the new design methodologies for multi-beam GRIN lenses. The radiation properties of designs using different methods are demonstrated and compared. Section III presents a design of the GRIN lens profile emulated by subwavelength unit cells. The feeding structure constituted by patch array modules is also illustrated. The prototype fabrication and measurement are reported in Section IV, and the results are compared with those from a full-wave analysis. Section V draws a conclusion.

II. 2-D Multi-beam GRIN Lens Design Theory

A typical lens with radially gradient refractive indices is depicted in Fig.1 (a). It is illuminated by a feed horn antenna located on the negative part of z-axis and radiates a boresight beam with enhanced realized gains. For multi-beam radiations, the conventional method is sketched in Fig.1 (b). The refractive-index profile on the GRIN lens is calculated for the boresight radiation (*Beam a*) with illuminations from *Feed a*.

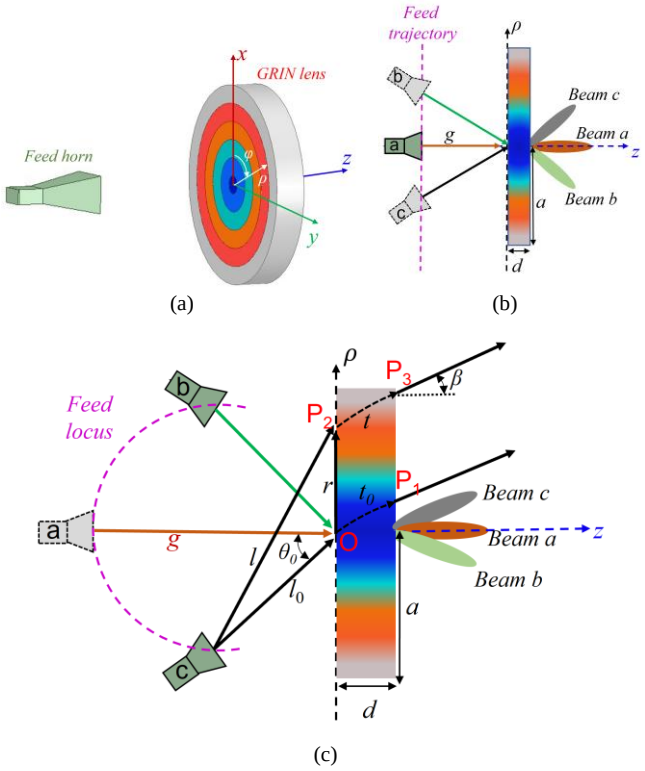

Fig. 1 Lens profile with radially gradient refractive indices (different colors on the lens aperture represent varied refractive indices). (a) 3-D configuration with one feed horn for boresight radiation. (b) Classical multi-beam configuration obtained by defocusing the feed of solution (a) in a φ plane, i.e., perpendicular to the lens surface. (c) Proposed multi-beam configuration in a φ plane, where the feed is on a spherical cup and the GRIN lens is designed by the maximum squinted beam.

Subsequently, by simply sliding the feed horn along a straight trajectory, oblique radiation beams (e.g., *Beam b* and *c*) can be realized since the ray paths from the focal point produce an

approximate linear phase on the lens aperture. However, as the feed is moved further away from the theoretical focal point (*Feed a*), the phase deviation with respect to the linear one provides a degradation of the beam, especially for large angles, as in any single focus system.

A. Radial-only GRIN Variation for Multi-beam Radiations

To significantly improve the multi-beam radiation performance, we propose a new GRIN lens design process as shown in Fig.1 (c). The lens still has radially gradient refractive indices. However, instead of calculating the refractive-index profile for the boresight beam, we calculate the profile for ideal symmetrical oblique beam radiations (*Beams b* and *c*) at the maximum radiation angles. To this end, consider the lens as illuminated by *Feed c* and the outgoing wave directed to an angle of β; the following condition should be satisfied to maintain constant optical ray-path lengths for any ray

$$l_0 + \int_O^{P_1} n(\rho)\, dt_0 + \left(r_{p3} - r_{p1}\right) sin\beta = l + \int_{P_2}^{P_3} n(\rho)\, dt, \tag{1}$$

where

P_1 is the exit point of the ray from lens center O,
l_0 is the focal length of O,
t_0 is the curvilinear abscise along the ray path from O to P_1,
P_2 is an arbitrary incident point on the lens at a radius r,
P_3 is the exit point on the output aperture corresponding to P_2,
r_{P3} and r_{P1} are the radii at points P_3 and P_1, respectively,
l is the focal distance of P_2,
t is the curvilinear abscise along the ray path from P_2 to P_3,
$n(\rho)$ is the refractive index related to a generic radius ρ.

To simplify the solution of (1), we first assume the ray paths in the lens are straight lines and have the same slope of the outgoing rays. Second, the refractive index along the ray path is calculated with the value at the incident point. It should be noted that these two assumptions are valid for a lens with small thickness d. This way, (1) can be simplified as

$$l_0 + n(0)\frac{d}{cos\beta} + rsin\beta = l + n(r)\frac{d}{cos\beta}. \tag{2}$$

The focal distance l can be obtained from

$$l = \sqrt{(l_0 cos\theta_0)^2 + (r + l_0 sin\theta_0)^2}, \tag{3}$$

where θ_0 represents the offset angle of *Feed c* with respect to z-axis. By defining n_Δ as the refractive index deviation with respect to the one in the origin, that is

$$n_\Delta = n(0) - n(r), \tag{4}$$

(2) can be rearranged as

$$l_0 + \frac{d}{cos\beta} n_\Delta + rsin\beta = \sqrt{(l_0 cos\theta_0)^2 + (r + l_0 sin\theta_0)^2}. \tag{5}$$

Applying square function to both sides of (5), leads to

$$\frac{d^2}{(cos\beta)^2} {n_\Delta}^2 + \frac{2l_0 d}{cos\beta} n_\Delta + 2rd\ tan\beta\ n_\Delta + 2rl_0\ sin\beta =$$

$$r^2 (cos\beta)^2 + 2rl_0 sin\theta_0. \tag{6}$$

The same derivations are now applied to *Feed b* and *Beam b*, which leads to swapping θ_0 and β with $-\theta_0$ and $-\beta$ in (6), that is

$$\frac{d^2}{(cos\beta)^2} {n_\Delta}^2 + \frac{2l_0 d}{cos\beta} n_\Delta - 2rdtan\beta n_\Delta - 2rl_0 sin\beta =$$

$$r^2 (cos\beta)^2 - 2rl_0 sin\theta_0. \tag{7}$$

Summation and subtraction of (6) and (7) leads to the equivalent couple of independent equations

$$\frac{d^2}{(cos\beta)^2} {n_\Delta}^2 + \frac{2l_0 d}{cos\beta} n_\Delta - r^2 (cos\beta)^2 = 0, \tag{8}$$

$$(d/\, l_0) tan\beta\ n_\Delta + sin\beta = sin\theta_0. \tag{9}$$

The above equations should be simultaneously satisfied. However, it can be seen in (9) that the angle θ_0 will depend on r through n_Δ; therefore, in the following procedure we will satisfy (9) in the average sense by integrating along r, while we will use (8) for finding n_Δ. Since n_Δ should be greater than 0, the solution of (8) in an arbitrary point on the lens can be obtained as

$$n_\Delta = \frac{\sqrt{{l_0}^2 + r^2 (cos\beta)^2} - l_0}{d/cos\beta}, \tag{10}$$

and therefore from (4)

$$n(r) = n(0) - \frac{\sqrt{{l_0}^2 + r^2 (cos\beta)^2} - l_0}{d/cos\beta}. \tag{11}$$

Once the lens dimensions and the desired maximal beam angles of $\pm\beta$ are defined, the refractive index $n(0)$ should be a constant value. It can be obtained by defining the edge refractive index as 1, i.e., $n(a) = 1$, where a is the lens radius; thus yielding

$$n(0) = 1 + \frac{\sqrt{{l_0}^2 + a^2 (cos\beta)^2} - l_0}{d/cos\beta}. \tag{12}$$

The feed offset angle θ_0 can be determined from the solution of (9) as

$$\theta_0(r) = \arcsin\left(sin\beta \left(1 + \frac{d n_\Delta}{l_0 cos\beta}\right)\right). \tag{13}$$

As mentioned, θ_0 is a function of r, rather than a fixed value, as desired. For example, let us consider a lens with a radius of a=2.5λ_0 (λ_0 is the wavelength in free space) and the desired maximal radiation angles of ±45°. The theoretical feed offset angle θ_0 for different lens positions are calculated and plotted in Fig. 2. First, for a constant ratio of lens thickness to its radius, i.e., d/a=0.3, θ_0 is calculated under different focal lengths, i.e., l_0/a. As shown in Fig. 2 (a), as the focal length increases, the

variation range of θ_0 becomes smaller. Besides, for a constant focal length of l_0/a=1.2, the feed offset angles θ_0 under different lens thickness are plotted in Fig. 2 (b). It is seen that the variation range of θ_0 only changes slightly for different lens thickness. It is varied from 45° to 52° when d/a=0.3 and l_0/a=1.2. Therefore, by carefully choosing the lens profile and the focal length, the theoretical offset angle can be approximated to a constant value. To determine the final offset angle of *Feed c* and *b*, a mean function is applied to obtain the average value for different lens positions; that is

$$\theta_0 = \frac{1}{a}\int_0^a \theta_0(r)dr. \quad (14)$$

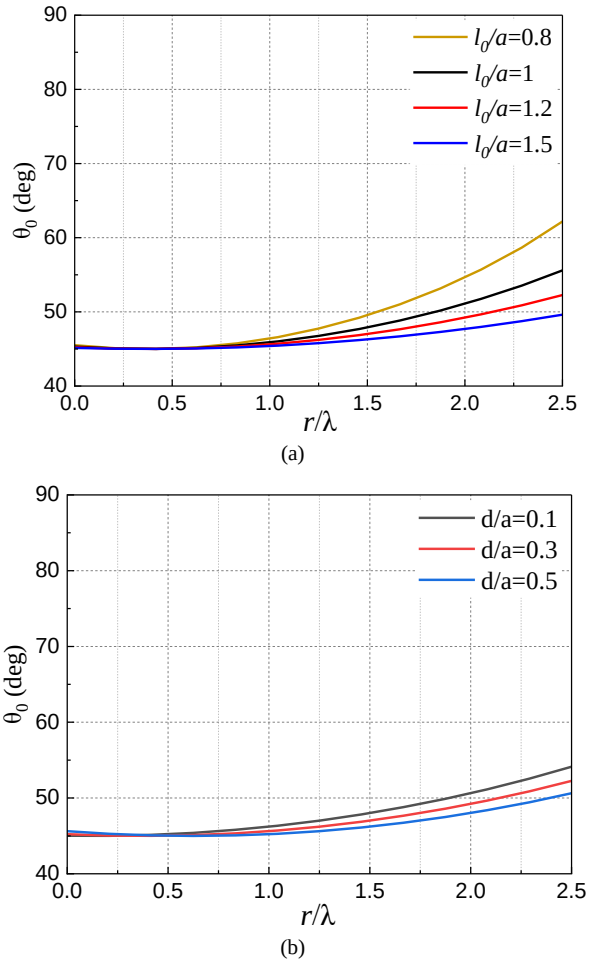

Fig. 2 Theoretical feed offset angles versus lens positions. (a) Different l_0/a with a constant d/a of 0.3. (b) Different d/a with a constant l_0/a of 1.2.

This means that (9) is not imposed rigorously, but in the average sense. The above analysis yields the refractive-index profile across the lens aperture. The corresponding feed positions for the maximum oblique radiations are determined with the focal length l_0 and the feed offset angles $\pm\theta_0$. The next step is to determine the position of *Feed a* for a boresight beam. As illustrated in Fig. 1 (c), an optimal focal length g can be found by moving the feed source along the z-axis, so that the average phase error on the aperture is minimized.

Finally, the locus of the feeds is determined by the circle passing from the 3 points corresponding to *Feeds a*, *b* and *c*. Multi-beam property will be realized by arranging multiple feeds on this locus. Since the lens refractive-index profile shows a rotational symmetry with respect to φ coordinate, as illustrated in Fig.1 (a), it can support beam-scanning/multi-beam radiations in different φ planes.

B. Radial-azimuthal GRIN Variation for Multi-beam Radiations

The multi-beam design process developed in Section II-A produces a lens with a radially gradient refractive-index profile as shown in Fig.1 (a), i.e., the refractive index remains the same along φ direction for a fixed radius. If multi-beam performance is required in one specific principal plane only, this solution can be improved by introducing an azimuthal GRIN variation. From (3), it is indeed noticed that the focal distance l for an arbitrary point on the lens was only considered to be dependent on the radius r, but this is true only if the observation point is in the feed-locus plane. As shown in Fig. 3, *Feed c* and *Feed b* are in *xoz* plane. The actual focal distance for points outside this plane, e.g., P_2, is related to both the radius r and the azimuthal angle φ_1.

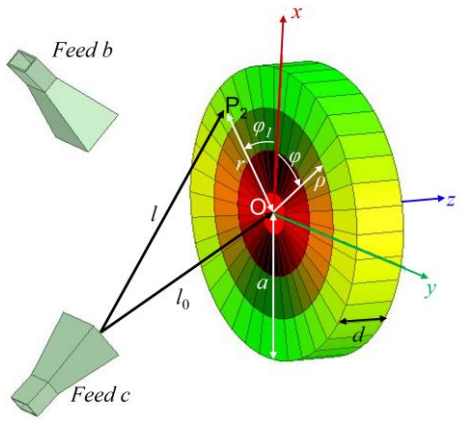

Fig. 3 Configuration of multi-beam lens with GRIN along both radial and φ directions for optimization of the multibeam performance in one plane.

To obtain a more accurate refractive-index profile for oblique maximal radiation beams, a lens with gradient refractive indices along both radial and azimuthal coordinates should be considered, as sketched in Fig. 3. The (x, y, z) coordinate of a ray footprint P_2 on the input lens interface is ($rcos\varphi_1$, $rsin\varphi_1$, 0). Two symmetric feeds are in *xoz* plane for two beams towards φ=0° and θ=$\pm\beta$, i.e., in directions $\hat{u} = \pm\sin(\beta)\hat{x} + \cos(\beta)\hat{z}$. Considering the equalization of optical ray-path lengths from *Feed c* (see Fig. 3), one can get

$$l_0 + n(0,0)\frac{d}{cos\beta} + rcos\varphi_1 sin\beta = l + n(r,\varphi_1)\frac{d}{cos\beta}. \quad (15)$$

The focal distance of P_2 can be calculated from

$$l = \sqrt{(l_0 sin\theta_0 + rcos\varphi_1)^2 + (rsin\varphi_1)^2 + (l_0 cos\theta_0)^2}. \quad (16)$$

The specular equation can be derived from the equalization of optical ray-path lengths with *Feed b* illuminations. By following the same derivation process discussed in Section II-

A, the refractive-index profile and the required feed offset angle can be obtained as

$$n(r,\varphi_1) = n(0,0) - \frac{\sqrt{{l_0}^2+r^2(1-(cos\varphi_1 sin\beta)^2)}-l_0}{d/cos\beta}, \quad (17)$$

$$\theta_0 = \frac{1}{2\pi a}\iint \arcsin\left(\left(1+\frac{d(n(0,0)-n(r,\varphi_1))}{l_0 cos\beta}\right) sin\beta\right) d\varphi_1 dr. \quad (18)$$

In (17), r and φ_1 are two independent variables, and $n(r, \varphi_1)$ has a minimal solution when $r=a$ and $\varphi_1=\pm\pi/2$, i.e., on the edge of the lens. By defining the minimal refractive index as 1, i.e., $n(a, \pm\pi/2)=1$, the constant $n(0,0)$ is calculated as

$$n(0,0) = 1 + \frac{\sqrt{{l_0}^2+a^2}-l_0}{d/cos\beta}. \quad (19)$$

We emphasize that the refractive index profile is related to both the radius r and the azimuthal angle φ_1, i.e., it does not have the rotational symmetry with respect to φ coordinate. Therefore, the radiation performance will change if the feed locus is rotated. However, the performance in the principal plane has been improved. It should be noted that the feed locus in *xoz* plane is determined from theoretical analysis to enhance the beam-scanning performance in this plane. There are phase errors on the lens aperture when rotating the *xoz*-plane feed locus to other azimuthal planes. The larger angle it is rotated by, the larger phase errors would appear. Due to the mirror symmetry of GRIN profile along x- and y-axes, the phase errors are maximal when the feed locus is rotated to *yoz* plane.

To compare the performance by a conventional method and the ones adopted here (in the two versions described in Section II-A and II-B), three lenses have been designed at 13 GHz based on GRIN dielectric substrates. A full-wave analysis is carried out on the three antennas by using ANSYS HFSS software simulator. Lens I is constructed referring to the traditional configuration in Fig.1 (b). Its refractive index profile is calculated from the ideal boresight radiation based on the closed form formula presented in [21]. Lens II is designed with the method presented in Section II-A, namely with radial-only GRIN variation calculated from ideal maximum oblique beams at $\pm\beta=\pm45°$. Lens III is designed with the method discussed in Section II-B, which is with radial-azimuthal GRIN, with same maximum squinted beams at $\pm\beta=\pm45°$ in *xoz* plane. All the lenses have the same physical dimensions, i.e., $a=2.5\lambda_0$, $d=0.3a$. The focal lengths of Lens II and III for ±45° radiations are both $l_0=a$. Their focal lengths for 0° are set as $g=1.47a$ for consistency. The focal length of Lens I for 0° is also chosen as $g=1.47a$. A standard gain horn LB75-15 from A-INFO is applied as the feed antenna for all three lenses. This horn has a realized gain of approximately 17.5 dBi at 13 GHz. The radiation performance of the three antennas is summarized in Table I. The three cases show similar gain at boresight. It should be considered however that Lens I is not designed for the maximum aperture efficiency as prescribed in [21] but assuming the same focal length, and thickness as those of Lenses II and III. The maximum radiation beam of Lens I from the traditional multi-beam design method can reach ±41°, showing a high sidelobe level of -2.7 dB and a high scanning loss of 4 dB in both *xoz* and *yoz* planes. The scanning loss in this work refers to the gain drop from the boresight beam to the largest oblique beams. By applying the new design method with radial-only GRIN profile, Lens II can support maximal radiation beams at ±44°. The sidelobe levels are reduced to -7.3 dB in both planes. The scanning loss also decreases to 2.2 dB in both planes. Finally, radial-azimuthal GRIN Lens III shows better performance in the designed plane (*xoz*), with a low sidelobe level of -10 dB and a low scanning loss of 0.8 dB at ±44°. However, the radiation performance in *yoz* plane deteriorates with a sidelobe level of -5 dB and a scanning loss of 2.5 dB at ±44°. Therefore, one can choose the design method of Lens II if balanced multi-beam radiations in different φ planes are desired. Nevertheless, if one prefers to maintain the best performance in one plane, the design method of Lens III can be chosen.

TABLE I
RADIATION PERFORMANCE OF GRIN LENSES FROM DIFFERENT METHODS

Model	Boresight Realized Gain (dBi)	Maximal oblique Beams (*xoz*/ *yoz* planes)			Scanning Losses (*xoz*/ *yoz* planes) (dB)
		Beam Angle	Realized Gain (dBi)	Sidelobe Level (dB)	
Lens I	22.7	±41°/±41°	18.7/18.7	-2.7/-2.7	4/4
Lens II	22.9	±44°/±44°	20.7/20.7	-7.3/-7.3	2.2/2.2
Lens III	22.2	±44°/±44°	21.4/19.7	-10/-5	0.8/2.5

III. SIMULATION RESULTS OF 2-D MULTI-BEAM GRIN LENS

To demonstrate the applicability of the developed method for multi-beam radiations, a GRIN lens is designed with a gradient refractive index along both radial and azimuthal coordinates referring to the analysis in Section II-B. The center operating frequency is 13 GHz. The lens has a radius of $a=57$ mm (around $2.5\lambda_0$) and a thickness of $d=12$ mm. The desired maximal squinted beams are at $\pm\beta=\pm50°$, and the corresponding focal lengths for them are $l_0=84$ mm. To calculate the refractive index profile, the lens aperture is divided evenly in 6 rings along the radial coordinate and in 36 sectors along the azimuthal coordinate. Following (17), the obtained refractive index has a variation range from 1.2 to 1.9, corresponding to a permittivity range from 1.4 to 3.6, as mapped in Fig. 4. Two feed positions for the maximum oblique beams can be determined with their offset angles of $\pm\theta_0 = \pm53°$ calculated from (18). Referring to Fig.1 (c), the feed for the boresight beam is located on negative z-axis with a focal length of g. Through full-wave simulations in HFSS, the optimal focal length is found as $g=100$ mm for a high realized gain. Subsequently, an arc of circle can be produced with three found feed positions. Multi-beam radiations can be achieved by placing multiple feeds along this arc and the feeds will face the lens center.

For this radial-azimuthal GRIN lens, *xoz* plane ($\varphi=0$) is selected as the principal beam-scanning plane as an example. Certainly, another azimuthal plane (for example, $\varphi=\alpha$) can be selected as the principal scanning plane. In this case, equations (17)-(19) are still valid. The permittivity distribution shown in Fig. 4 and the feed loci only need to be rotated by α. This way,

the beam scanning performance in the $\varphi = \alpha$ plane will be the same as that in the *xoz* plane of the current design.

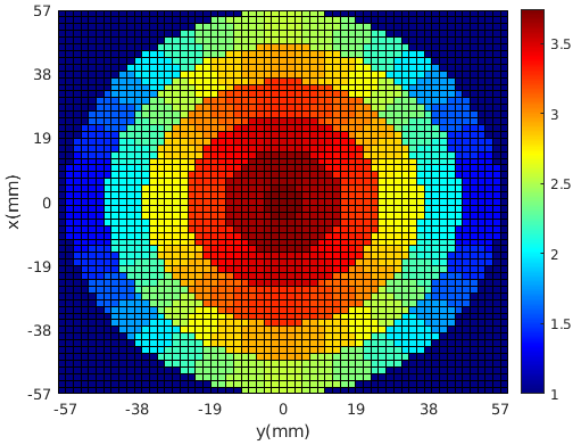

Fig. 4 Permittivity distribution of the designed 2-D multi-beam GRIN lens.

A. Unit Cell

As an alternative to a GRIN dielectric lens, we have used here multilayer metasurfaces with variable local impedances. To meet the effective medium assumption [38]-[39] and enable a wideband property, the periodicity of the unit cell on the surface is subwavelength. The proposed unit cell model is illustrated in Fig. 5. It consists of three circular metal patches printed on two identical substrates of Rogers RO4003 (ε_r=3.55, tan δ=0.0027) with equal thicknesses h_s=0.203 mm. An air box with a height of h_0=2 mm is added under the substrate to reduce the effective permittivity of the unit cell. The total thickness of the unit cell including the airbox is 2.406 mm. The effective permittivity is calculated by characterizing transmission coefficients from the top metal layer to the bottom of the air box. The periodicity of the unit cell is P=2 mm (less than $\lambda_0/10$). The three round metal patches of one unit cell have the same radius r_p, which is varied from 0.1 mm to 0.9 mm to tune the transmission properties and effective permittivity.

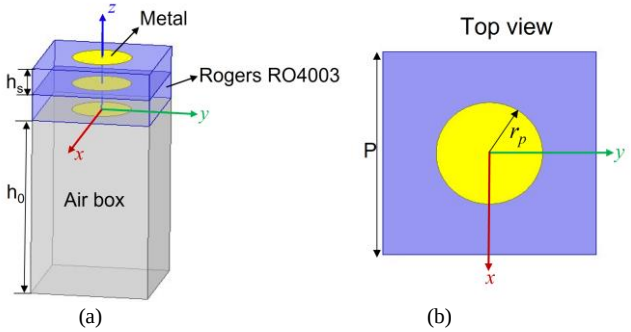

Fig. 5 Unit cell model. (a) 3-D view. (b) Top view.

3-D EM simulations of the unit cell are carried out in ANSYS HFSS. Periodic boundaries are assigned along both x- and y-axes, and two Floquet ports are added on the positive and negative z-axis, respectively. Fig. 6 (a) shows the simulated transmission coefficients of the unit cell with different patch radii under normal incidences. It is noticed that the transmission losses are less than 3 dB from 8 GHz to 15 GHz for all unit cells. Referring to the retrieval process reported in [39], the corresponding effective permittivity values of unit cells with different parameters are calculated and compared in Fig. 6 (b).

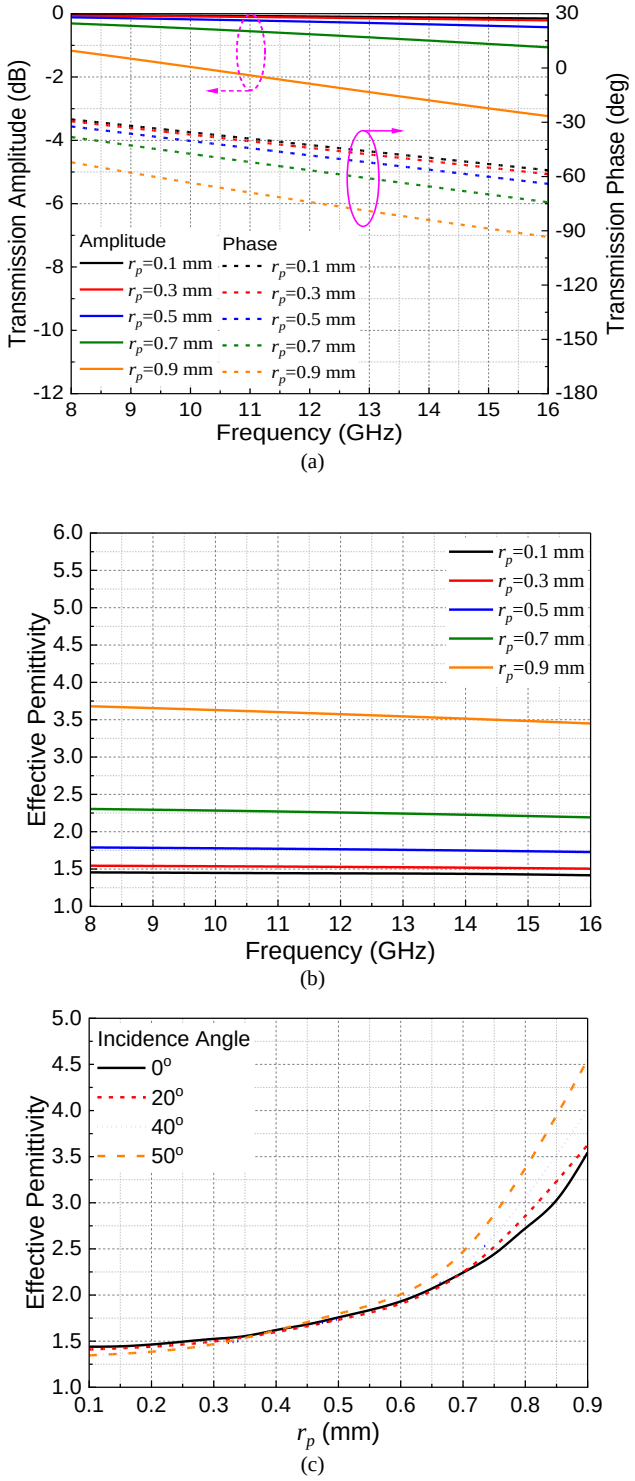

Fig. 6 Simulation results of unit cell. (a) Transmission coefficients under normal incidence. (b) Effective permittivity versus frequency under normal incidence. (c) Effective permittivity versus patch radius at 13 GHz under different incident angles.

The effective permittivity of each unit cell is stable from 8 GHz to 15 GHz, and it is varied for different values of r_p. Fig. 6 (c)

presents the effective permittivity versus r_p at 13 GHz for different incident angles of the unit cells. Under normal incidence, the equivalent relative permittivity ranges from 1.4 to 3.6. It is also seen that it is very stable with the angle tilt when the unit cells have less than 0.7 mm radii, namely $\lambda_0/33$ at 13 GHz. It should be noted that the required permittivity range on the lens aperture will be larger for a smaller lens thickness. For a given lens thickness, its permittivity range should fall within the achievable range of the unit cell. Considering the specific unit cell model in this work, the lens should be thicker than 12 mm to meet the permittivity range of the unit cell (i.e., 1.4-3.6). In this work, we chose the lens thickness as 12 mm as an example. However, if a thinner lens is desired, the unit cell model should be changed accordingly for a larger permittivity variation range. The permittivity values of unit cell can be increased by multiple methods, such as reducing the air gap thickness or using a substrate with a higher dielectric constant.

B. Feed Antenna

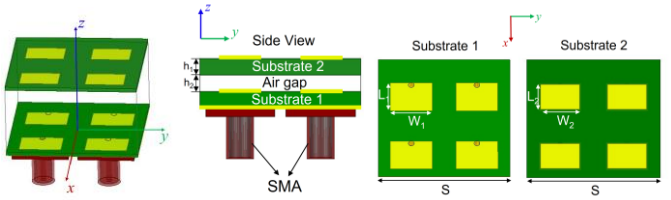

(a) (b) (c)

Fig. 7 Basic module of the feed patch array antenna. (a) Exploded view. (b) Side view. (c) Top views of two substrates. (Green color represents substrate; yellow color is metal.)

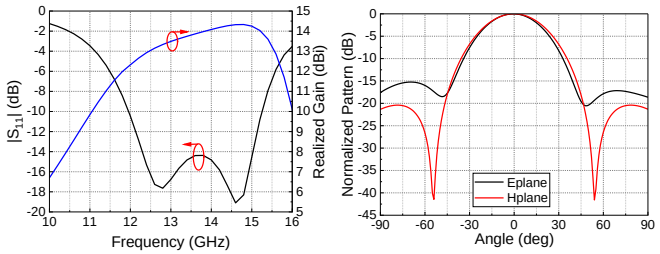

(a) (b)

Fig. 8 Simulated results of feed array antenna. (a) Reflection coefficient and realized gain versus frequency. (b) Normalized radiation patterns at 13 GHz.

It is complicated and bulky to arrange multiple gain horns on the curved feed locus to illuminate the GRIN lens. We adopt therefore the light and simple solution constituted by a conformal microstrip patch array. Fig. 7 shows the basic module, consisting of a 2×2 array of rectangular patches with parasitic elements printed on a superstrate. The latter has the purpose to increase the bandwidth. Both the driving and the parasitic patches are printed over Rogers RT/duroid 5880 (ε_r=2.2, tan δ=0.0009, thickness h_1=0.787 mm) with a side length S=30 mm; they are separated by an air gap of thickness h_2=1mm. The 2×2 driving patches are fed by four coaxial cables. Each patch has a dimension of $L_1 \times W_1$=7 mm×9.4 mm. The 2×2 parasitic patch dimensions are $L_2 \times W_2$=6.2 mm×8.6 mm.

The simulated reflection coefficient of a single port versus frequency is given in Fig. 8 (a). It is below -10 dB from 12 GHz to 15.3 GHz, showing therefore a bandwidth of 24.2%. Since all four ports are identical, only one port results are shown here. Besides, the realized gain of the patch array with the same phase and amplitude of the elements is also plotted in Fig. 8 (a). The peak realized gain value is 14.3 dBi at 14.7 GHz. The 3-dB gain bandwidth is 30.7% from 11.6 GHz to 15.8 GHz. The normalized radiation patterns along both E- and H- planes at 13 GHz are shown in Fig. 8 (b). The 10-dB beamwidth of them are similar and around ±33°.

C. Numerical Analysis of the Overall Structure

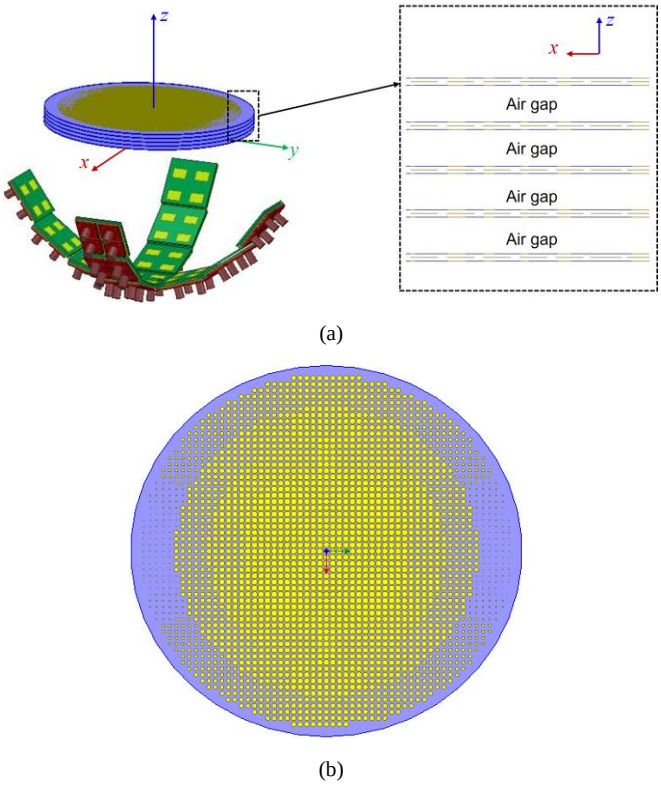

(a)

(b)

Fig. 9 (a) Whole configuration of the 2-D multi-beam GRIN lens. (b) Schematic diagram of the lens upper surface.

TABLE II
FEED POSITIONS FOR MULTI-BEAM RADIATIONS

Feed No.	Feed offset angle	Focal length/mm
1	0°	100
2	18°	98
3	36°	92
4	53°	84

The configuration of the designed 2-D multi-beam GRIN lens is shown in Fig. 9. Different sized unit cells from Section III-A are arranged on different areas of the GRIN lens aperture to achieve the desired refractive-index profile. To achieve a 12-mm-thick lens aperture, 5 layers of the 2.406-mm-thick unit cell are applied (see inset of Fig. 9). Simulation results find that the mutual couplings between each layer are negligible. Seven patch array modules as the one described in Section III-B are positioned on the focal loci in *xoz* and *yoz* planes, respectively. Considering the symmetry, the focal lengths and feed offset angles with respect to z-axis for the four feeds in half *xoz*/yoz plane are listed in Table II.

Multi-beam radiation patterns of the unit-cell implemented lens and the ideal pure-dielectric lens have been simulated at 13 GHz using ANSYS HFSS, as plotted in Fig. 10 (a) and (b). For

the final implemented lens, the boresight beam has a peak gain of 21.8 dBi, corresponding to an aperture efficiency of 63%. The maximal oblique radiation beams in *xoz* and *yoz* planes are obtained at ±46° and ±45°, respectively. The beam-scanning losses in *xoz* and *yoz* planes are 2.1 dB and 3.6 dB, respectively. It is noticed that the multi-beam patterns from the two lenses agree well with each other, except that the directed beam angles of the unit-cell implemented lens are slightly smaller than the ones from the ideal lens. This is due to the refractive-index errors when applying periodic unit cells to mimic the material with ideal permittivity, especially under large oblique incidence.

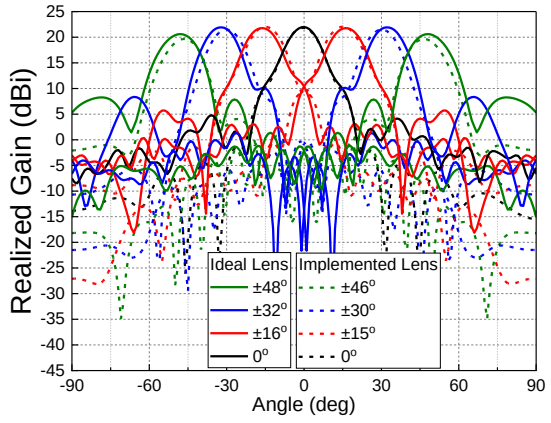

(a)

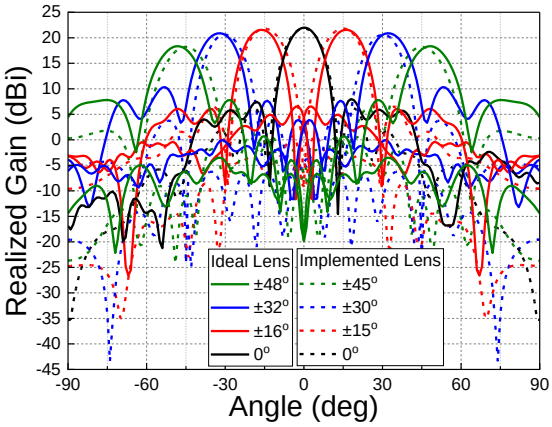

(b)

Fig. 10 Simulated multi-beam radiation patterns at 13 GHz. (a) *xoz* plane. (b) *yoz* plane.

IV. Fabrication and Measurement

A prototype of the 2-D multi-beam GRIN lens described in Section III-C is fabricated and measured, as shown in Fig. 11. The lens aperture includes five printed circuit boards separated by four 2-mm-thick spacers. Each circuit board consists of two laminated substrates of Rogers RO4003. The feed antenna from Section III-B is manufactured using Rogers RT/duroid 5880. Two substrates are separated by a 1-mm-thick spacer. Four SMAs are soldered to the bottom side of the lower substrate.

Subsequently, 13 feed antennas are assembled and fixed onto two focal loci that are fabricated using 3-D printing technology. The fixture for mounting the lens to the measurement platform is made of Aluminum. The final multi-beam GRIN lens structure is shown in Fig. 11.

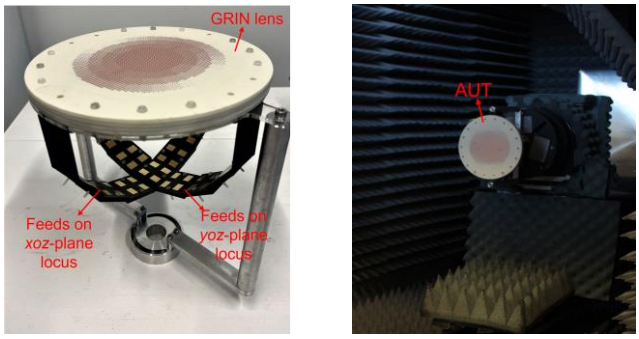

(a) (b)

Fig. 11 (a) Fabricated prototype. (b) The prototype under test.

For the measurement, a one-to-four commercial power divider is connected to four SMAs of one feed array antenna. The antenna array can also be fed by an integrated power divider, which is not shown here for brevity. The input reflection coefficients of a single feed patch element and GRIN lens for multiple beams are measured using a Keysight Vector Network Analyzer (VNA) N5225A. As given in Fig. 12, the experimental results of $|S_{11}|$ for different radiation beams are mostly below -10 dB from 12 GHz to 15 GHz, coinciding with the designed frequency bandwidth of the feed antenna from Section III-B. Due to the symmetry of the whole structure, Fig. 12 only shows the data of positive beams for clarity.

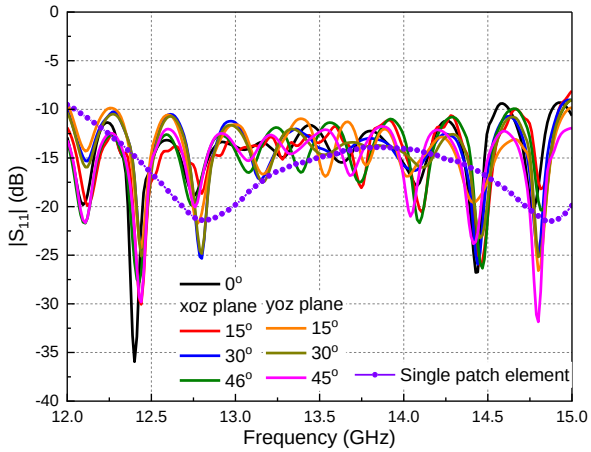

Fig. 12 Measured input reflection coefficients of different beams.

As shown in Fig. 11 (b), far field radiation patterns of the prototype are measured in a Microwave Vision Group (MVG) compact range located at University of Technology Sydney, Australia. The measured radiation patterns at 13 GHz are normalized and compared with the simulated counterparts in Fig. 13. It is observed that the main radiation beams from simulation and measurement agree reasonably well. The measured highest sidelobe levels are -9 dB for the beams at ±46° in *xoz* plane and -7 dB for the beams at ±45° in *yoz* plane, respectively. The measured cross-polarized radiation patterns at 13 GHz are normalized with respect to the corresponding co-polarized beams in both *xoz* and *yoz* planes, as given in Fig. 14. It can be noticed that all of them are lower than -20 dB.

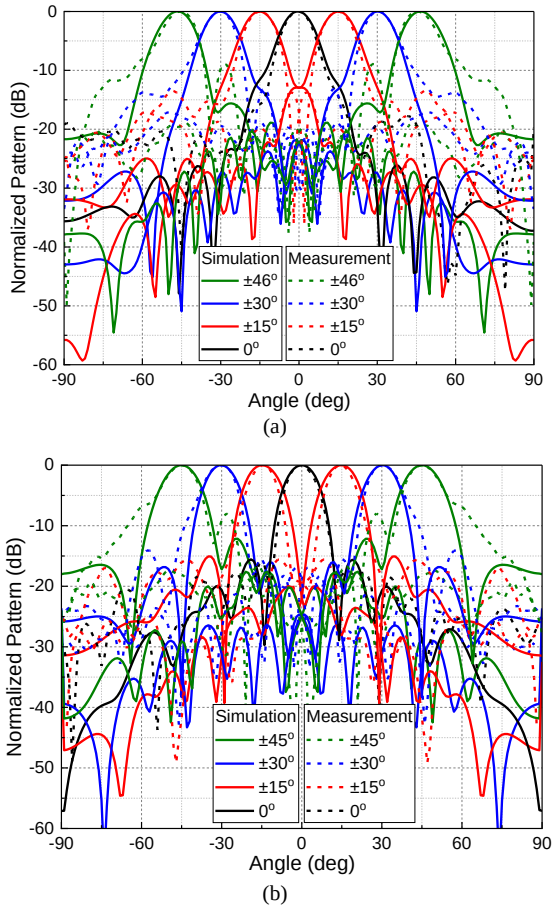

Fig. 13 Simulated and measured normalized radiation patterns at 13 GHz. (a) *xoz* plane. (b) *yoz* plane.

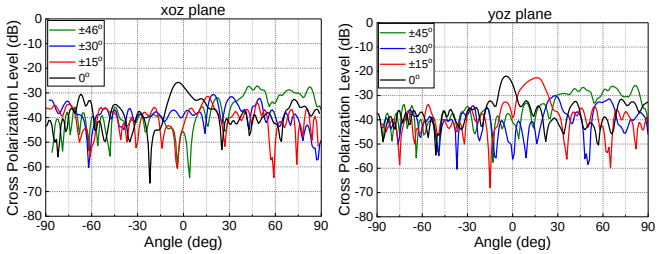

Fig. 14 Measured cross polarization levels of multiple beams in both *xoz* and *yoz* planes.

The measured peak realized gains and aperture efficiencies versus frequency in terms of different beams in *xoz* and *yoz* planes are plotted in Fig. 15 (a) and (b), respectively. The maximal gain value of the boresight beam is 22.3 dBi at 13.4 GHz, corresponding to an aperture efficiency of 66.4%. The aperture efficiency is defined as the ratio of the gain and the maximum directivity of the array aperture, and the latter is obtained as 4π times the physical aperture area on square wavelength. It is noticed that the aperture efficiencies for large angles are lower. This can be attributed to two main reasons. First, during the lens synthesis process with approximations, there are some phase errors on the aperture, especially for tilted beams in yoz plane. This will cause gain drops with a consequence of low aperture efficiencies. Second, the deviations of effective permittivity of unit cell under oblique incidences will lead to gain drops and low aperture efficiencies for beams titled to large angles. The scanning losses in *xoz* plane from 0° to ±46° are 1-2.6 dB aross the frequency band from 12 GHz to 15 GHz. The scanning losses in *yoz* plane from 0° to ±45° are 2.1-3.9 dB. For each beam, its realized gain variations in the operating frequency band from 12 GHz to 15 GHz are less than 3 dB. Besides, multi-beam radiation patterns at other frequency points in both *xoz* and *yoz* planes are normalized and plotted in Fig. 16 (a)-(c). Stable multi-beam radiation properties with beam coverages of around ±45° have been achieved in both *xoz* and *yoz* planes from 12 GHz to 15 GHz.

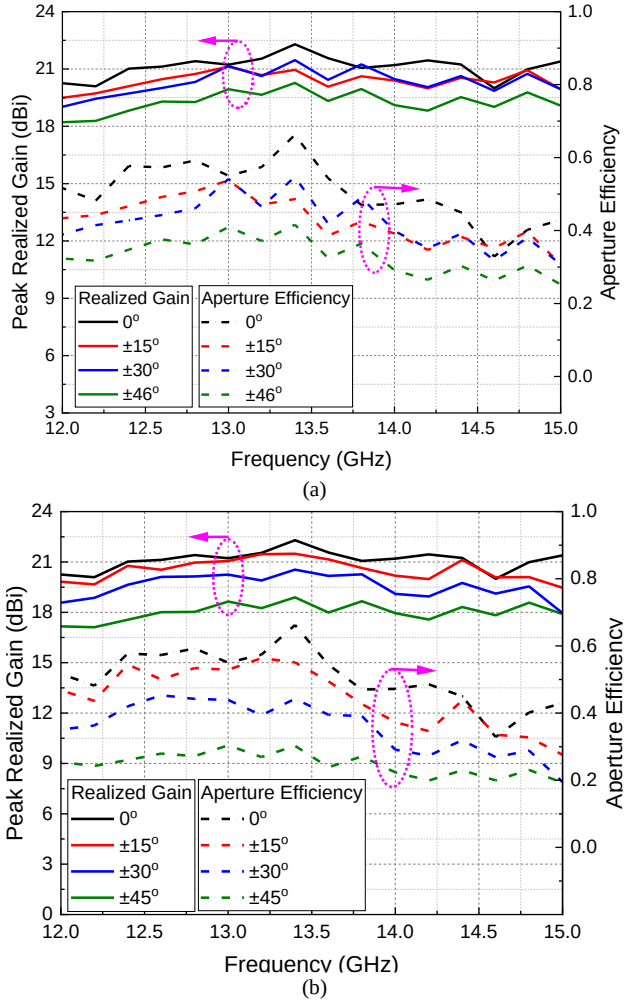

Fig. 15 Measured peak realized gain and aperture efficiency versus frequency. (a) Multiple beams in *xoz* plane. (b) Multiple beams in *yoz* plane.

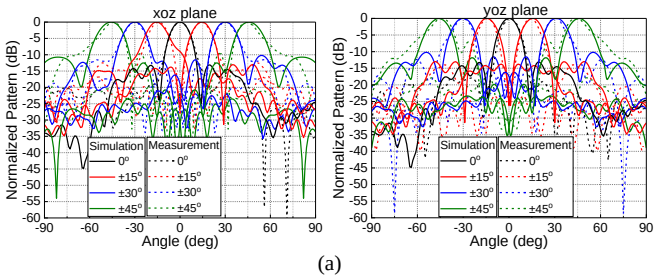

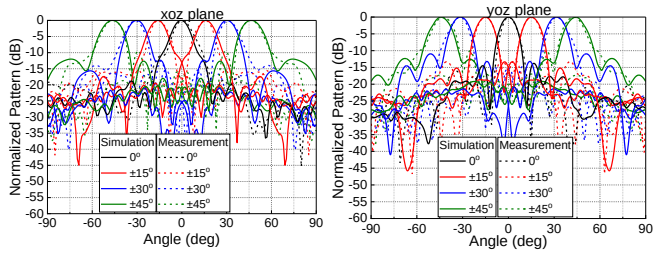

(b)

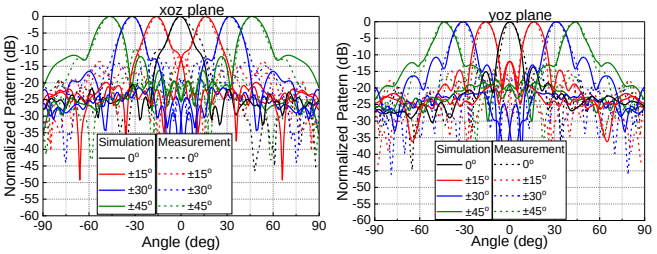

(c)

Fig. 16 Normalized multi-beam radiation patterns in *xoz* and *yoz* planes. (a) 12 GHz. (b) 14 GHz. (c) 15 GHz.

Table III compares the radiation performance of the developed multi-beam flat GRIN lens with other reported flat lenses. It is noticed that the lenses in [29] and [33] can provide a high aperture efficiency of greater than 60%. But they have either a small beam-scanning range or a high scanning loss. Besides, they require large effective permittivity ranges for lens apertures, leading to challenges of unit-cell designs and final lens implementations. On the other hand, the designs from [28], [30]-[31] have comparable/ larger beam scanning ranges and low scanning losses. Nevertheless, their aperture efficiencies are lower than 40%. Moreover, all the reported designs were for 1-D beam scanning. The developed lens in this work outperforms others as it can enable a high aperture efficiency, a wide 2-D scanning range and a low scanning loss.

TABLE III
PERFORMANCE COMPARISONS WITH OTHER REPORTED DESIGNS

Ref.	Freq. (GHz)	ε_r range	Beam range (°)	Scanning Loss (dB)	Aperture efficiency (%)	Scanning Dimensions
[28]	10	1.01-13.3	±54°	0.7/2.2	21.2	1-D
[29]	10	2.1-12.35	±34°	2	67	1-D
[30]	8.5	1.1-7.6	±45°	3	38	1-D
[31]	60	2.25-6.05	±48°	4.6	27.4	1-D
[32]	28	/	±27°	3.7	24.5	1-D
[33]	18	1.5-7.1	±53°	5.5	74%	1-D
This work	13.4	1.4-3.6	±46°	2/3.4	66.4%	2-D

V. CONCLUSION

A 2-D wide-angle multi-beam flat GRIN lens is presented with a high aperture efficiency. New design methods are developed to calculate the refractive-index profile across the lens aperture and the feed positions. Multiple beams can be realized by placing multiple feed antennas on a circular locus. Moreover, a 2-D multi-beam flat GRIN lens is constructed, with 13 feed sub-array modules arranged in *xoz* and *yoz* planes. Stable multi-beam radiations are realized from 12 GHz to 15 GHz, covering an angular range of around ±45° with low scanning losses in both *xoz* and *yoz* planes. The measured peak aperture efficiency is 66.4%.

REFERENCES

[1] Y. J. Guo, M. Ansari, R. W. Zilkowski and N. J. G. Fonseca, "Quasi-optical multi-beam antenna technologies for B5G and 6G mmwave and THz networks: a review," *IEEE Open Journal of Antennas and Propagation*, vol. 2, pp. 807-830, 2021.

[2] P. -Y. Qin, L. -Z. Song and Y. J. Guo, "Conformal transmitarrays for unmanned aerial vehicles aided 6G networks," *IEEE Commun. Mag.*, vol. 60, no. 1, pp. 14-20, Jan. 2022.

[3] D. González-Ovejero, G. Minatti, G. Chattopadhyay and S. Maci, "Multi-beam by Metasurface Antennas," *IEEE Trans. Antennas Propag.*, vol. 65, no. 6, pp. 2923-2930, Jun 2017.

[4] F. Yang, S. Yang, Y. Chen, S. Qu and J. Hu, "Convex optimization of pencil beams through large-scale 4-D antenna arrays," *IEEE Trans. Antennas Propag.*, vol. 66, no. 7, pp. 3453-3462, July 2018.

[5] O. Quevedo-Teruel, J. Miao, M. Mattsson, A. Algaba-Brazalez, M. Johansson, L. Manholm, "Glide-symmetric fully metallic Luneburg lens for 5G communications at Ka-band," *IEEE Antennas Wireless Propag. Lett.*, vol. 17, no. 9, pp. 1588-1592, Sep. 2018.

[6] Y. Li, L. Ge, M. Chen, Z. Zhang, Z. Li, J. Wang, "Multibeam 3-D-printed Luneburg lens fed by magnetoelectric dipole antennas for millimeter-wave MIMO applications," *IEEE Trans. Antennas Propag.*, vol. 67, no. 5, pp. 2923-2933, May 2019.

[7] X. Zhang, F. Yang, S. Xu and M. Li, "Single-layer reflectarray antenna with independent dual-CP beam control," *IEEE Antennas Wireless Propag. Lett.*, vol. 19, no. 4, pp. 532-536, Apr. 2020.

[8] L.-Z. Song, P.-Y. Qin, H. Zhu and J. Du, "Wideband conformal transmitarrays for E-band multi-beam applications," *IEEE Trans. Antennas Propag.*, early access, 2022.

[9] Z. H. Jiang, Y, Zhang, W, Hong, "Anisotropic impedance surface-enabled low-profile broadband dual-circularly polarized multibeam reflectarrays for Ka-band applications," *IEEE Trans. Antennas Propag.*, vol. 68, no. 8, pp. 6441-6446, Aug. 2020.

[10] H. Zhu, M. Ansari and Y. Jay Guo, "Wideband beam-forming networks utilizing planar hybrid couplers and phase shifters," *IEEE Trans. Antennas Propag.*, vol. 70, no. 9, pp. 7592-7602, Sep. 2022

[11] J.-W. Lian, Y.-L. Ban, C. Xiao, Z.-F. Yu, "Compact substrate-integrated 4×8 Butler matrix with sidelobe suppression for millimeter-wave multibeam application," *IEEE Antennas Wireless Propag. Lett.*, vol. 17, no. 5, pp. 928-932, May 2018.

[12] A. Papathanasopoulos, Y. Rahmat-Samii, N. C. Garcia and J. D. Chisum, "A novel collapsible flat-layered metamaterial gradient-refractive-index lens antenna," *IEEE Trans. Antennas Propag.*, vol. 68, no. 3, pp. 1312-1321, Mar. 2020.

[13] G. -B. Wu, Y. -S. Zeng, K. F. Chan, S. -W. Qu and C. H. Chan, "3-D printed circularly polarized modified Fresnel lens operating at terahertz frequencies," *IEEE Trans. Antennas Propag.*, vol. 67, no. 7, pp. 4429-4437, Jul. 2019.

[14] J. Xu, Z. N. Chen, and X. Qing, "270-GHz LTCC-integrated high gain cavity-backed Fresnel zone plate lens antenna," *IEEE Trans. Antennas Propag.*, vol. 61, no. 4, pp. 1679–1687, Apr. 2013.

[15] H. -X. Xu, G. -M. Wang, Z. Tao and T. Cai, "An octave-bandwidth half Maxwell fish-eye lens antenna using three-dimensional gradient-index fractal metamaterials," *IEEE Trans. Antennas Propag.*, vol. 62, no. 9, pp. 4823-4828, Sep. 2014.

[16] H. F. Ma, B. G. Cai, T. X. Zhang, Y. Yang, W. X. Jiang and T. J. Cui, "Three-dimensional gradient-index materials and their applications in microwave lens antennas," *IEEE Trans. Antennas Propag.*, vol. 61, no. 5, pp. 2561-2569, May 2013.

[17] K. Liu, C. Zhao, S. -W. Qu, Y. Chen, J. Hu and S. Yang, "A 3-D-printed multibeam spherical lens antenna with ultrawide-angle coverage," *IEEE Antennas Wireless Propag. Lett.*, vol. 20, no. 3, pp. 411-415, Mar. 2021.

[18] C. Wang, J. Wu and Y. -X. Guo, "A 3-D-printed multibeam dual circularly polarized Luneburg lens antenna based on quasi-Icosahedron models for Ka-band wireless applications," *IEEE Trans. Antennas Propag.*, vol. 68, no. 8, pp. 5807-5815, Aug. 2020.

[19] O. Quevedo-Teruel, W. Tang, R. Mitchell-Thomas, et al, "Transformation optics for antennas: why limit the bandwidth with metamaterials?" *Sci. Rep.* 3, p. 1903, May 2013.
[20] I. Aghanejad, H. Abiri and A. Yahaghi, "Design of high-gain lens antenna by gradient-index metamaterials using transformation optics," *IEEE Trans. Antennas Propag.*, vol. 60, no. 9, pp. 4074-4081, Sep. 2012.
[21] A. Paraskevopoulos, F. Maggiorelli, M. Albani and S. Maci, "Radial GRIN lenses based on the solution of a regularized ray congruence equation," *IEEE Trans. Antennas Propag.*, vol. 70, no. 2, pp. 888-899, Feb. 2022.
[22] F. Maggiorelli, A. Paraskevopoulos, J. C. Vardaxoglou, M. Albani and S. Maci, "Profile inversion and closed form formulation of compact GRIN lenses," *IEEE Open J. Antennas Propag.*, vol. 2, pp. 315-325, 2021.
[23] S. Zhang, R. K. Arya, W. G. Whittow, D. Cadman, R. Mittra and J. C. Vardaxoglou, "Ultra-wideband flat metamaterial GRIN lenses assisted with additive manufacturing technique," *IEEE Trans. Antennas Propag.*, vol. 69, no. 7, pp. 3788-3799, Jul. 2021.
[24] Q. -W. Lin and H. Wong, "A low-profile and wideband lens antenna based on high-refractive-index metasurface," *IEEE Trans. Antennas Propag.*, vol. 66, no. 11, pp. 5764-5772, Nov. 2018.
[25] N. Garcia, and J. Chisum, "Reduced dimensionality optimizer for efficient design of wideband millimeter-wave 3D metamaterial GRIN lenses," *Microw. Opt. Technol. Lett.* vol. 63, no. 5, pp.1372-1376, May 2021.
[26] S. Jain, M. Abdel-Mageed and R. Mittra, "Flat-lens design using field transformation and its comparison with those based on transformation optics and ray optics," *IEEE Antennas Wireless Propag. Lett.*, vol. 12, pp. 777-780, 2013.
[27] T. Li and Z. N. Chen, "Compact wideband wide-angle polarization-free metasurface lens antenna array for multibeam base stations," *IEEE Trans. Antennas Propag.*, vol. 68, no. 3, pp. 1378-1388, Mar. 2020.
[28] Y. Su, Z. N. Chen, "A radial transformation-optics mapping for flat ultra-wide-angle dual-polarized stacked GRIN MTM Luneburg lens antenna," *IEEE Trans. Antennas Propag.*, vol. 67, no. 5, pp. 2961-2970, May 2019.
[29] C. Mateo-Segura, A. Dyke, H. Dyke, S. Haq and Y. Hao, "Flat Luneburg lens via transformation optics for directive antenna applications," *IEEE Trans. Antennas Propag.*, vol. 62, no. 4, pp. 1945-1953, Apr. 2014.
[30] S. M. A. M. H. Abadi and N. Behdad, "Design of wideband, FSS-based multibeam antennas using the effective medium approach," *IEEE Trans. Antennas Propag.*, vol. 62, no. 11, pp. 5557-5564, Nov. 2014.
[31] M. Imbert, A. Papió, F. De Flaviis, L. Jofre and J. Romeu, "Design and performance evaluation of a dielectric flat lens antenna for millimeter-wave applications," *IEEE Antennas Wireless Propag. Lett.*, vol. 14, pp. 342-345, 2015.
[32] M. Jiang, Z. N. Chen, Y. Zhang, W. Hong and X. Xuan, "Metamaterial-based thin planar lens antenna for spatial beamforming and multibeam massive MIMO," *IEEE Trans. Antennas Propag.*, vol. 65, no. 2, pp. 464-472, Feb. 2017.
[33] N. Garcia, W. Wang, and J. Chisum, "Feed corrective lenslets for enhanced beamscan in flat lens antenna systems," *Opt. Express*, vol. 30, no. 8, pp.13047-13058, Apr. 2022.
[34] A. L. Peebles, "A dielectric bifocal lens for multibeam antenna applications," *IEEE Trans. Antennas Propag.*, vol. 36, no. 5, pp. 599-606, May 1988.
[35] T. V. La, N. T. Nguyen, M. Casaletti and R. Sauleau, "Design of medium size dielectric bifocal lenses for wide angle beam scanning antennas," *6th European Conference on Antennas and Propagation (EUCAP)*, Prague, Czech Republic, pp. 3287-3291, 2012.
[36] F. Holt and A. Mayer, "A design procedure for dielectric microwave lenses of large aperture ratio and large scanning angle," IRE *Trans. Antennas Propag.*, vol. 5, no. 1, pp. 25-30, Jan. 1957.
[37] L.-Z. Song, P.-Y. Qin, T. Zhang, J. Du, Y. J. Guo, "High-efficiency multi-beam GRIN lens with 2-D wide-angle coverages," *5th Australian Microwave Symposium*, Feb. 2023.
[38] D. R. Smith, et al, "Electromagnetic parameter retrieval from inhomogeneous metamaterials." *Physical review E*, 71, no. 3, Mar. 2005.
[39] D. R. Smith, et al, "Determination of effective permittivity and permeability of metamaterials from reflection and transmission coefficients," *Physical review B*, 65, no. 19, Apr. 2002.